Journal of the European Ceramic Society 45 (2025) 116801

Contents lists available at ScienceDirect

Journal of the European Ceramic Society

journal homepage: www.elsevier.com/locate/jeurceramsoc

Isothermal oxidation of bulk dense Fe_2AlB_2 and Mn_2AlB_2 phases in 700–1000 °C temperature range

Tarek Aly ElMeligy [a,b], Or Messer [c], Maxim Sokol [c], Mary Qin Hassig [a], Michel W. Barsoum [a,*]

[a] *Department of Materials Science & Engineering, Drexel University Philadelphia, PA 19104, USA*
[b] *Department of Mechanical Engineering, The British University in Egypt, Cairo, Egypt*
[c] *Department of Materials Science and Engineering, Tel Aviv University, Ramat Aviv 6997801, Israel*

ARTICLE INFO

Keywords:
Transition metal borides
MAB phases
Layered solids
Oxidation
High-temperature

ABSTRACT

Herein, the isothermal oxidation of Mn_2AlB_2 and Fe_2AlB_2 MAB phases in air was studied. When oxidized at 700 °C, the weight gain kinetics for Mn_2AlB_2 are sub-cubic up to 96 h as a result of the formation of a $Mn_{2-x}Al_xO_3$ protective layer. Severe spallation of the oxides formed was observed at 800 °C and 900 °C, limiting its service temperature. The oxidation kinetics at 900 °C, for Fe_2AlB_2 become sub-parabolic beyond 60 h due to the formation of a passivating $Al_4B_2O_9$ with excellent corner adherence. At both 800 °C and 1000 °C, however, the oxidation is rapid and severe. Therefore, both Mn_2AlB_2 and Fe_2AlB_2 may be used in practical application up to 700 °C and 900 °C, respectively. As far as we are aware, Fe_2AlB_2 is the second transition metal boride that is oxidation resistant at 900 °C; the first, MoAlB, is also a MAB phase.

1. Introduction

Layered ternary transition metal boride (MAB) phases, where M is a transition metal (mostly group 6–8), A is Al, and B is boron, have garnered increasing attention owing to their unique properties [1]. They crystallize with different structural chemistries. The MAB phases studied herein, Mn_2AlB_2 and Fe_2AlB_2, have a M_2AB_2 (space group Cmmm) chemistry. Becher et. al [2] discovered Mn_2AlB_2; Jeitschko [3] and Kuz'ma [4] discovered Fe_2AlB_2. According to Ade and Hillebrecht [5], the MAB structure consists of M-B blocks of face-sharing BM_6 trigonal prisms interleaved with either A-atom planes or intermetallic A layers.

We present the current, though limited, research related to the effect of oxygen partial pressure on the thermal stability as well as the oxidation behavior of the Mn_2AlB_2 and Fe_2AlB_2 phases, respectively. Kota et al. [6] investigated the thermal stability of Mn_2AlB_2 and reported it peritectically decomposed into the binary MnB and Al-based intermetallic $Al_{10}Mn_3$ at $T > 1100$ °C in nitrogen (N_2) and at $T \sim 1100$ °C in argon (Ar) atmospheres. Cedervall et al. [7] investigated $(Fe_{1-x}Mn_x)_2AlB_2$ substitutional solid-solution and showed a decrease in decomposition temperature under Ar from 1242 °C at $x = 0$, to ~1200 °C at $x = 0.5$ to ~1100 °C at $x = 1$. Said otherwise, the addition of Mn reduces the stability of Fe_2AlB_2.

Liu et. al. [8] reported that Fe_2AlB_2 also peritectically decomposes in an Ar atmosphere at $T = 1236$ °C into FeB, $FeAl_3$, and AlB_{12}. Verger et al. [9] concluded that HCl-treated Fe_2AlB_2 powder decomposed - at temperatures as low as 600 °C in N_2 atmospheres - into FeB, AlN and some small amounts of α−alumina, α-Al_2O_3. These results are consistent with those of Kota et al. [10]. The large variations in decomposition temperature between bulk samples and powders under different atmospheres highlights that the thermal stability of Fe_2AlB_2 is kinetics-limited.

There has been no work on the high-temperature oxidation behavior of Mn_2AlB_2 or Fe_2AlB_2. Benamor et al. [11] demonstrated friction-wear tribo-oxidation by dry-sliding Mn_2AlB_2 against different ceramic and steel components. The dry sliding of Mn_2AlB_2 across WC, Al_2O_3, and Si_3N_4 resulted in tribo-oxidation and Raman signals for Mn_3O_4 and MnO_2 in the tribo-oxides.

One of the factors affecting the adhesion of oxide films is the thermal expansion mismatch between the oxide and substrate. Using *in situ* high-temperature, x-ray diffraction (XRD), Verger et al. [9] reported the linear thermal expansion coefficients (CTEs) of Mn_2AlB_2 and Fe_2AlB_2 to be 14.0×10^{-6} K^{-1} and 10.3×10^{-6} K^{-1}, respectively. For Al_2O_3 and Al_5BO_9 the average CTEs are 8.5×10^{-6} K^{-1} and 6.1×10^{-6} K^{-1}, respectively [12,13].

The aim of this work is to report, to the best of our knowledge, for the first time on the bulk isothermal oxidation behavior of the Mn_2AlB_2 and

---

* Correspondence to: 3141 Chestnut Street, LeBow 444, Philadelphia, PA 19104, USA.
E-mail address: barsoumw@drexel.edu (M.W. Barsoum).

https://doi.org/10.1016/j.jeurceramsoc.2024.116801
Received 24 March 2024; Received in revised form 2 August 2024; Accepted 2 August 2024

Fe_2AlB_2 MAB phases to evaluate their maximum service temperature in practical applications.

2. Materials and methods

2.1. Synthesis

The samples were synthesized by mixing the appropriate reagents in the molar ratios listed in Table 1. The detailed synthesis procedure for Mn_2AlB_2 has been described elsewhere [6]. In brief, the reactant powders with the molar compositions listed in Table 1 were ball-milled for 24 h with a 1:1 wt ratio of ZrO_2 milling balls. Fe, Al, and B powders were mixed in the same method. The powders were inserted into a 38.1 mm diameter graphite die, coated with boron nitride (BN) as a release spray and layered with graphite foil. The Mn_2AlB_2 powders were stacked on top of their Fe counterparts, with a graphite spacer between them. The powder mixtures were reactively hot-pressed (HPed) under a load corresponding to a pressure of ~ 36 MPa applied 15 min after reaching the dwell temperature. The heating rate was 6.7 °C/min, with a dwell time of 2 h at 1050 °C. After furnace cooling, the surfaces of the samples were ground using coarse diamond pads (120 grit) to remove any residual graphite foil bonded to the surface.

2.2. Oxidation tests

The HPed Mn_2AlB_2 and Fe_2AlB_2 samples were diamond cut and electrically discharge machined (EDM) into $8.2 \times 4.8 \times 3.2$ mm^3 and $8.4 \times 4.4 \times 2.9$ mm^3 rectangular slabs for the box-furnace tests, respectively. The thermogravimetric analysis (TGA) test samples were machined to $4.1 \times 4.8 \times 3.2$ mm^3 and $4.2 \times 4.8 \times 3.2$ mm^3, respectively. Prior to the oxidation tests each slab was polished with 400–1200 grit SiC paper to remove machining residue and improve the surface finish

Two types of oxidation tests were carried out: the first used a box furnace, and the second used TGA. In the former, the samples were placed in Al_2O_3 crucibles and heated, in air in a box furnace, at 5 °C/min to 700, 800, 900, and 1000 °C. The heating rate was chosen to minimize transient oxidation during heating while mitigating thermal shock. After a prescribed oxidation time at the various temperatures, the alumina crucible were removed from the furnace and weighed. Said otherwise, we used one sample per time interval and temperature.

The TGA oxidation experiments were carried out at room temperature (RT) and above, utilizing Labsys by Setarem operating in continuous mode, with α-Al_2O_3 crucibles. The measurements were carried out in continuous mode at 800–1000 °C at 10 °C/min with a 15–96 h isothermal hold at the soak temperature in simulated air (20/80 oxygen/nitrogen mixture by volume). We used a faster heating rate for the TGA than for the box furnace to minimize the rapid oxidation transient during heating. The TGA samples were smaller, allowing for faster heating without significant thermal gradients within the sample. The TGA instrument provided precise and rapid thermal control, enabling faster heating rates without overshooting the soak temperature. For each oxidation experiment, two runs were carried out at each oxidation temperature. The first run was carried out with an empty crucible as a baseline correction, while the second run was carried out with a sample in the crucible. TGA weight gain curves were corrected by subtracting the first run from the second run.

Table 1
Specifications of powders and processing parameters used for synthesis of Mn_2AlB_2 and Fe_2AlB_2, respectively. All powders were procured from Alfa Aesar.

Reagent	Moles	Purity (metal basis)	Particle Size (μm)
Al	1.2	99.5 %	≤ 44
B[a]	2	98.0 %	≤ 44
Mn	2	99.6 %	≤ 10
Fe	2	98.0 %	≤ 44

[a] Crystalline and amorphous.

2.3. Characterization

XRD patterns were obtained using a powder diffractometer (SmartLab, Rigaku Corp., Tokyo, Japan) with Cu-Kα radiation in Bragg Brentano scan mode. XRD patterns of the bulk Mn_2AlB_2 and Fe_2AlB_2 samples were obtained before and after oxidation. The samples were scanned in the $2\theta = 10$–70 ° range, with a step size of 0.02 ° and a dwell time of 4 s per step.

Rietveld refinement was conducted using the BGMN suite within the Profex user interface in the $2\theta = 15$–$65°$ range [14,15]. The diffractometer's instrumental peak-shape function parameters were determined by using a lanthanum hexaboride (LaB_6) standard (NIST 660b). Details of the BGMN refinement model are provided in the Supplementary Information. The refined parameters are the background coefficients, profile shape, sample displacement, phase fractions, scale factors with preferred orientation correction, crystallite size, and lattice parameters, LPs. Refinement results were evaluated by weighted profile R-factor, R_{wp}, statistically expected R-factor, R_{exp} and reduced chi-squared, χ^2 (see Fig. S5-S12 and Table S2)

The fractured oxidized samples were cold-mounted in epoxy and ground, first using 240–1200 SiC grit paper, and then down to 1 μm with a diamond suspension. Micrographs and elemental compositions, of mostly cross-sectional maps, were obtained using a scanning electron microscope, SEM (Zeiss Supra 50 VP, Carl Zeiss SMT AG, Oberkochen, Germany), equipped with an energy-dispersive X-ray spectroscope, EDS, (Oxford EDS, Oxfordshire, United Kingdom). The EDS was calibrated using an Al_2O_3 reference. The EDS values reported represent a combination of spot and area scans selected from various regions on the samples polished to 1 μm. An accelerating voltage of 12–20 kV and a 60 s dwell times were used for the EDS measurement at a 15 mm working distance and 30–60 μm aperture size. The phase fractions of the various phases were determined from SEM micrographs using the ImageJ software package. The reported phase fractions represent the average of 3 measurements on various parts of the sample using image contrast, which was then converted to weight percentages.

XPS spectra were recorded using a photometer (VersaProbe 5000, Physical Electronics, Chanhassen, Minnesota, USA). The samples were analyzed before and after Ar+ sputtering. The sputtering was carried out using a 2.00 kV Ar+ ion beam for 60 s. The samples were mounted on an Al stub via carbon tape. Monochromatic Al-Kα X-rays, with a pass energy of 23.50 eV, a step size of 0.50 eV, 0.2 s step time and a spot size of 200 μm, were used to irradiate the sample surfaces. Five scans were obtained for each region. The CasaXPS Version 2.3.23PR1.0 software was used for peak fitting and chemical compositional analysis. The obtained spectra were calibrated by setting the valence-band edge to zero. This was performed by fitting the valence edge with a step-down function and setting the intersection to 0.00 eV [16]. The C 1 s spectra were calibrated to a binding energy, BE, of 285.00 eV. The oxide peaks were fitted using a symmetric Gaussian/Lorentzian line shape. The background was determined using the Shirley algorithm.

3. Results and discussion

3.1. Composition and structure

SEM micrographs of the polished, reactively HPed samples (Fig. 1) confirmed that the samples were dense with small amounts of impurity phases. In the Mn-based samples, the EDS chemistry is $Mn_2Al_{0.92}B_2$ and the main impurities were 5±5 wt% Al_2O_3 and 2±5 wt% $MnAl_{1.80}$ (Fig. 1a). The composition of the B element is assumed to be in accordance with its theoretical stoichiometry. The detected Al_2O_3 was a result of the aluminothermic reduction of native metal oxides present on the precursor powders.

In the Fe-case, the EDS chemistry is $Fe_2Al_{1.02}B_2$. In this case, the main

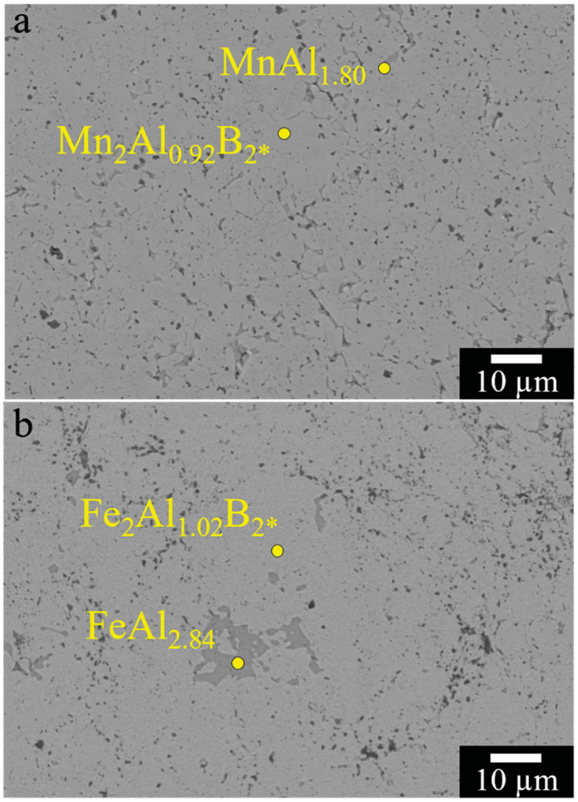

Fig. 1. Cross-sectional, backscattered electron SEM micrographs of hot-pressed, a) Mn_2AlB_2, and b) Fe_2AlB_2 samples. * B composition is assumed to be the stoichiometric value.

impurity was 8±5 wt% $FeAl_{2.84}$ (Fig. 1b). Here again, the composition of the B element is assumed to be in accordance with its theoretical stoichiometry.

Before discussing the oxidation results in detail, it is important to note that at temperatures $>$ 700 °C, the Mn_2AlB_2 oxide layers spalled quite readily (See Table 2). Thus, in what follows, most of the discussion will focus on the 700 °C oxidation test, where no spallation was observed. The other results are shown in Supplementary Information (Figs. S3, and Table S1).

The XRD patterns of the Mn_2AlB_2 and Fe_2AlB_2 samples oxidized in the 700–1000 °C temperature range (see Fig. 2a-b and Figs. S1-S2) showed the formation of multiple oxides. Detailed phase fractions obtained by Rietveld refinement are found in the Supplementary Information (see Fig. S5). In the case of Mn_2AlB_2 oxidized at 700 °C for 6 h, the main phase observed was Mn_2O_3. Additionally, a smaller fraction of Mn_2BO_4 was detected, as indicated by the ratio of the highest peak for Mn_2O_3 (at $\sim$32.9 °) to Mn_2BO_4 (at $\sim$33.5 °) in Fig. 2a and Fig. S1.

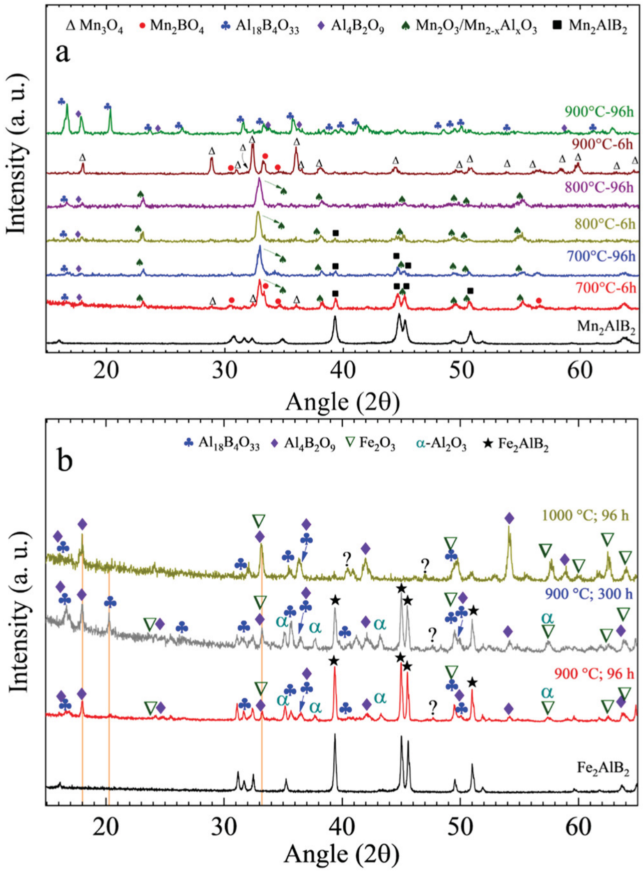

Fig. 2. XRD patterns of unoxidized and oxidized samples of, a) Mn_2AlB_2 in the 700–900 °C temperature range at various times indicated on figure, and b) Fe_2AlB_2 at 900 C for 96 h and 300 h and after 1000 °C for 96 h.

Table 2
List of observed spallation for oxidized Mn_2AlB_2 and Fe_2AlB_2 samples at 700–1000 °C after 6–300 h.

Mn_2AlB_2			Fe_2AlB_2		
Temp. (°C)	Time (h)	Spallation	Temp. (°C)	Time (h)	Spallation
700	6, 24 & 48	No	800	96	Minor
800	48, 96 & 150	Yes	900	96, 300	No
900	6, 48, 96	Severe	1000	96	Minor
1000	15	Reacted with crucible			

The presence of some Mn_3O_4 cannot be discounted at this time. This oxide layer was thin enough that the underlying Mn_2AlB_2 substrate peaks were detectable. After 96 h of oxidation at 700 °C (blue pattern in Fig. 2a), the substrate and Mn_3O_4 peaks diminished with no major changes in the oxide species formed. Peaks corresponding to Mn_2BO_4 were also present (Figs. S1a and S1b).

For Mn_2AlB_2 and up to 96 h of oxidation, the oxide species at 800 °C matched those at 700 °C, albeit with little Mn_3O_4 peaks at 800 °C (Fig. 2a and Fig. S1c). Whereas for Fe_2AlB_2, at 800 °C and 1000 °C the oxidation was severe and rapid (Fig. S4) with no detectable α−Al_2O_3 formation (Fig. 2b).

For Mn_2AlB_2, at an increased temperature of 900 °C, after 6 h (Fig. S1e) of oxidation, the dominant crystalline oxide phase became Mn_3O_4 (Fig. 2a and Fig. S1e). After 96 h of oxidation at 900 °C (Fig. 2a and S1f), the predominant oxide formed was $Al_{18}B_4O_{33}$, with some Mn_3O_4 also present. Conversely, for Fe_2AlB_2 at 900 °C, clear evidence of the formation α−Al_2O_3 is present at all times, in addition to peaks corresponding to the substrate (Fig. 2b and Fig. S2a-b). However, some peaks remained unidentified. After oxidation for 300 h, peaks corresponding to the $Al_{18}B_4O_{33}$ phase became more prominent (Fig. 2b and Fig. S2b). Remarkably, strong peaks corresponding to the substrate persisted after 300 h of oxidation at 900 °C (Fig. 2b and Fig. S2b).

After oxidation at 1000 °C for 96 h, clear evidence for the formation of the $Al_4B_2O_9$ and Fe_2O_3 phases was observed; the Al_2O_3 peaks disappeared and the $Al_{18}B_4O_{33}$ peaks were greatly reduced (Fig. 2b and Fig. S2c). The presence of $Al_4B_2O_9$ (i.e. $2Al_2O_3{\cdot}B_2O_3$) and the disappearance of Al_2O_3 (Fig. 2b and Fig. S2c) is an important result because it indirectly implies the presence of B_2O_3 followed by a subsequent reaction between it and Al_2O_3.

3.2. Oxidation kinetics

The time, *t,* dependence of the mass gain per unit area, *ΔW/A*, obtained from the box furnace (Fig. 3a-b) and the TGA (inset of Fig. 3b) was analyzed through power law kinetics, assuming the following relationship was operative,

$$\frac{\Delta W}{A} = k' t^{n} \tag{1}$$

where *k'* and *n* are the power law rate constant and rate exponent, respectively. The TGA oxidation results for Mn_2AlB_2 at 800–1000 °C were severe and rapid and were therefore omitted. The area-normalized weight gain curves of Mn_2AlB_2, on a linear scale at 700 °C, are shown in Fig. 3a. The same results plotted on a log scale are shown in the inset of Fig. 3a. From the inset, the rate exponent is calculated and listed in Table 3 to be 0.13, which is remarkably low, suggesting that the oxidation halts at 700 °C. It follows that at this temperature, Mn_2AlB_2 is oxidation resistant for at least 96 h.

As discussed later, from XPS analysis (Table 4) we conclude that after 6 h, the oxide formed is $Mn_{1.85}Al_{0.15}O_3$. If that is the case, then it is reasonable to conclude that the oxidation reaction at the lower temperatures is:

$$Mn_2AlB_2 + 3.73\ O_2 \rightarrow Mn_{1.85}Al_{0.15}O_3 + 0.075\ Mn_2BO_4 + 0.425\ Al_2O_3 + 0.96\ B_2O_3 \tag{2}$$

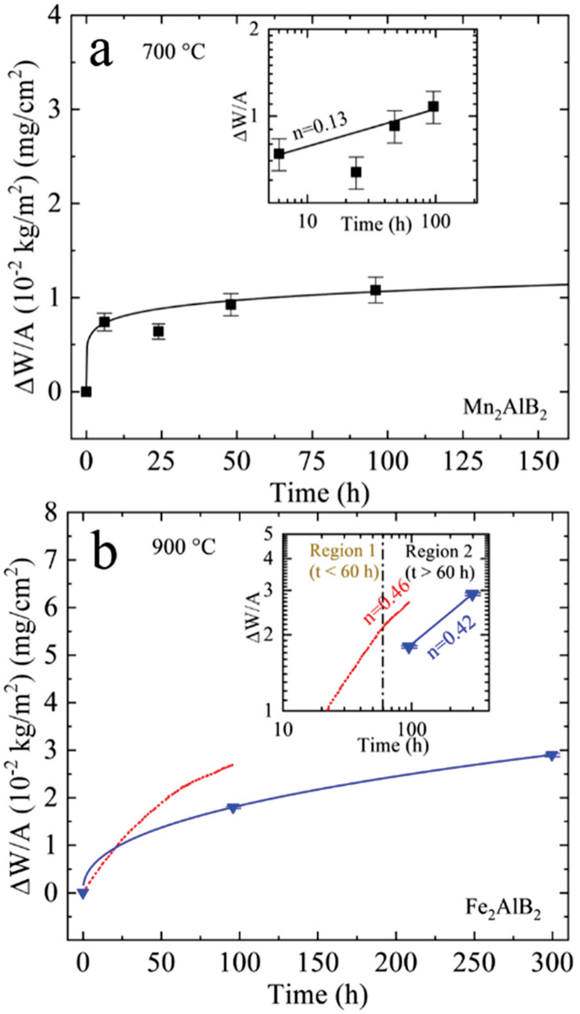

Fig. 3. Weight gain per unit area for, a) Mn_2AlB_2 and b) Fe_2AlB_2. Furnace runs are shown as solid lines linking individual data points. Insets show the same as a and b in logarithmic scale. The TGA results are shown by red dashed lines.

Table 3
Oxidation weight gain rate constants and exponents derived by least-squares regression fitting of experimental results (Fig. 3) for Mn_2AlB_2 and Fe_2AlB_2.

	Power Law				
Sample	Time (h)	T (°C)	k' [c]	n	R^2
Mn_2AlB_2 [a]	> 6	700	6.0± 1.0	0.13± 0.02	97 %
Fe_2AlB_2 [a]	> 96	900	2.6± 0.1	0.42± 0.01	-
Fe_2AlB_2 [b]	> 60	900	3.3± 0.1	0.46±0.01	99 %
Fe_2AlB_2 [b]	< 60	900	0.7± 0.1	0.85±0.01	99 %

[a] Furnace

[b] TGA

[c] $\times 10^{-3}$ kgm$-^{2}$s^{-n}

Table 4
XPS surface chemical composition after sputtering for oxidized Mn_2AlB_2 at 700 °C after 6 h and Fe_2AlB_2 at 900 °C after 24 h as compared to corresponding EDS composition (last column).

Substrate	Element	After Sputter (at%)	Matched phase	
			From XPS	From XRD and SEM
Mn_2AlB_2	C	7.1	$Mn_{2\text{-}x}Al_xO_3$ + small amount of B_2O_3	$Mn_{2\text{-}x}Al_xO_3$ +Mn_2BO_4
	O	57.1		
	B	5.0		
	Al	4.3		
	Mn	26.6		
$Fe_2AlB_2^{‡}$	O 1s	62	$Al_4B_2O_9 + B_2O_3$	Fe_2O_3 +Al_2O_3 + $Al_4B_2O_9$
	Al 2p	25		
	B 1s	13		

‡ The Fe signal in the XPS after oxidation was quite low.

or more generally,

$$Mn_2AlB_2 + 1/8\ (30\text{-}x)\ O_2 \rightarrow Mn_{2\text{-}x}Al_xO_3 + x/2\ Mn_2BO_4 + (1/2 - x/2)\ Al_2O_3 + (1 - x/4)\ B_2O_3 \tag{3}$$

At 900 °C, and presumably higher temperatures, the Al_2O_3 and B_2O_3 react to yield $Al_4B_2O_9$ which modifies the reaction to:

$$Mn_2AlB_2 + 3.73\ O_2 \rightarrow Mn_{1.85}Al_{0.15}O_3 + 0.075\ Mn_2BO_4 + 0.21\ Al_4B_2O_9 + 0.75\ B_2O_3 \tag{4}$$

Note these reactions *cannot* be balanced without the formation of B_2O_3 *and* Al_2O_3. The absence of any XRD evidence for Al_2O_3 suggests that it dissolves in the $Mn_{2\text{-}x}Al_xO_3$ phase. At 700 °C, the solubility of Al in Mn_2O_3 is ≈ 34±2 at% [17,18].

At higher temperatures, the Mn oxidation state shifts from +3 towards +2.67; a shift that is consistent with the fact that at 1 atm, Mn_3O_4, rather than Mn_2O_3, is the stable oxide [19–22]

Reactions 2–4 account for the fact the majority phase, at short times, is $Mn_{2\text{-}x}Al_xO_3$, with smaller amounts of Mn_2BO_4 (Figs. 2a and 4a). At longer times, a de-mixing of sorts occurs, where a Mn-rich oxide phase is found near the surface and an Al-rich one is found near the oxide/substrate interface (Fig. 4c). It is currently unclear whether these oxides have the same structure. Demixing also takes place in other oxides like (Ni,Co)O and (Mg,Co)O, as described by Yurek and Schmalzried [23–26].

Schmalzried explained that when a homogeneous solid solution of (A,B)O is exposed to an oxygen activity gradient, it leads to a flux of cation vacancies, causing kinetic demixing. This defect flux results in two outcomes: (1) the entire crystal shifts towards the side with higher oxygen activity, even though the oxygen ions are practically immobile. (2) Because the hopping frequency of a vacancy to a neighboring cation site is higher for one cation species than the other, the vacancy flux transports the faster cations towards the side with higher oxygen activity, where vacancies are formed at the sample surface, leading to demixing. A steady-state demixing profile is established after a period of

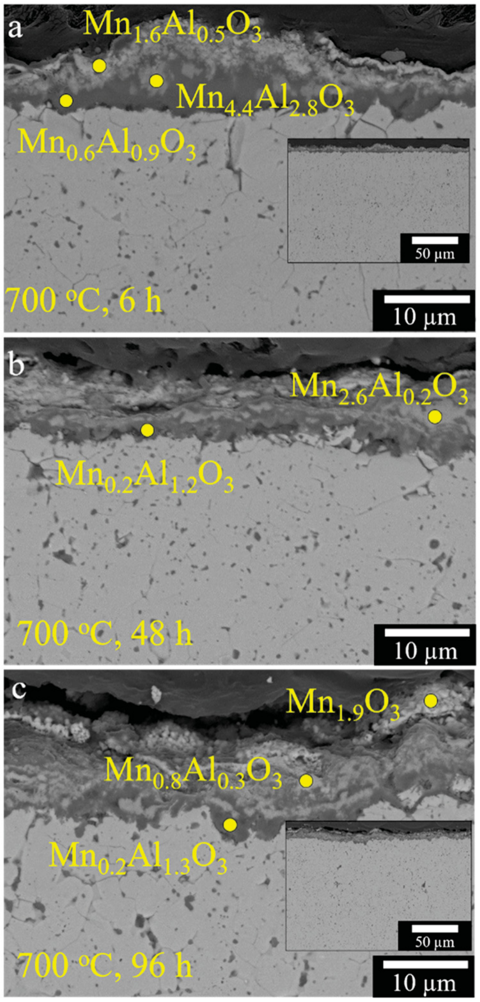

Fig. 4. Backscattered electron SEM micrographs of oxidized Mn_2AlB_2 polished cross-sections after oxidation in ambient air at 700 °C after 6 h to 96 h as indicated in the panels. Insets are lower magnification micrographs.

incubation. The diffusional flux of cations down their concentration gradient is counterbalanced by the uphill flux of the faster cations caused by the vacancy flux in the oxygen potential gradient.

After oxidizing Mn_2AlB_2 at 900 °C for 96 h, two ternary compounds, $Al_{18}B_4O_{33}$ and $Al_4B_2O_9$, were formed. In our previous work we showed the structural similarity between various MAB phases [1]. In the MoAlB case, the oxidation product was also identified as $Al_{18}B_4O_{33}$, and the formation and evaporation of B_2O_3 was assumed [12]. There is no evidence to suggest otherwise in the Mn_2AlB_2 case as well. Details on the influence of B_2O_3 evaporation as predicted by the chemical reactions are found in the Supplementary Information and Fig. S13. This comment notwithstanding, the exact contribution of B_2O_3 to the oxidation kinetics presented herein would require mass spectroscopic investigation and is outside the scope of this work.

In most of our work on the MAX phases [27–29], and now the MAB phases, the main reason why some of them are oxidation resistant is the selective oxidation of Al, which leads to the formation of an Al_2O_3 layer. It is thus interesting to note that, reactions 2–4 notwithstanding, at short times, the oxides formed – $Mn_{2\text{-}x}Al_xO_3$ and Mn_2BO_4 – are *not* alumina based. In that sense, this is new.

For Fe_2AlB_2, somewhat surprisingly, at 900 °C, a passivating oxide did form. The oxidation kinetics (Fig. 3b) of this compound appear to change at $t \approx 60$ h. At shorter times, $n = 0.85$, and is thus relatively high (inset in Fig. 3b). At $t > 60$ h, with n values between 0.42 and 0.46 (inset of Fig. 3b, Table 3) the kinetics are subparabolic and consistent with the formation of a passivating $\alpha{-}Al_2O_3$ up to 300 h of oxidation (Fig. 5a and d).

According to the XRD results, at shorter times and lower temperatures, Al_2O_3 and Fe_2O_3 are present. If one also ignores Fe-based oxide solid solutions, then a simplified oxidation reaction for Fe_2AlB_2 at 900 °C is

$$4\ Fe_2AlB_2 + 15\ O_2 \rightarrow 4\ Fe_2O_3 + 2\ Al_2O_3 + 4\ B_2O_3 \quad (5)$$

At 1000 °C, Al_2O_3 and B_2O_3 reacted to form $Al_4B_2O_9$ for the overall reaction:

$$4\ Fe_2AlB_2 + 15\ O_2 \rightarrow 4\ Fe_2O_3 + Al_4B_2O_9 + 3\ B_2O_3 \quad (6)$$

At temperatures of 900 °C, and higher, B_2O_3 is presumed to evaporate. [30,31]

3.3. Scale morphologies and phase composition

For the Mn_2AlB_2 composition after 6 h of oxidation at 700 °C, a multiphasic oxide layer formed. For the most part, the thickness of that layer was 3±2 µm (inset of Fig. 4a). In some regions, however, thicker mounds, ≈ 10 µm thick, formed (Fig. 4a). After 48 h of oxidation, a 9 ±2 µm thick oxide layer formed (Fig. 4b). Extending the oxidation to 96 h, slightly increased the thickness of the multiphase oxide layer (Fig. 4c). At longer oxidation times, the thicknesses of the oxide layer were more uniform (e.g. inset of Fig. 4c)

Before discussing the scale compositions determined by EDS, it is important to note that the oxide scales formed are multiphasic, and at such a fine scale, it is difficult to pinpoint the exact phases formed. The presence of B in some of these oxide layers (see Fig. 2 and Fig. S1), which cannot be quantified using EDS, adds another layer of complexity. To address this problem in what follows, and in the various micrographs shown herein, we simply list the chemistries obtained from EDS. This comment notwithstanding, the darkest regions shown in Fig. 4a, b and c tentatively match Al_2O_3.

The results of the EDS measurements are shown on Fig. 4 and Fig. S3. For reasons that are not understood, some compositions appear to be improbable. Looking at the totality of the results (Fig. 4 and Fig. S3) the following are important points: i) the outer oxides are Mn-rich and Al-poor; ii) layers adjacent to the substrate are Al-rich and in many cases can be identified as Al_2O_3; iii) the intermediate layers contain roughly equal amounts of Al and Mn.

Comparing these results with the XRD patterns (Fig. 2a), we conclude that, at short times, the Mn atoms react with O first forming Mn_2O_3/$Mn_{2\text{-}x}Al_xO_3$ and Mn_2BO_4. At higher temperatures and longer times, Mn_2BO_4 disappears and is replaced by Mn_3O_4 (Fig. 2a and Fig. S1). Simultaneously, alumina-rich phases, $Al_{18}B_4O_{33}$ and/or $Al_4B_2O_9$, form near the oxide/substrate interface. Based on the oxidation kinetics these oxide layers render Mn_2AlB_2 oxidation resistant at 700 °C.

Analysis of the substrate grains underneath the oxide (Fig. S3g) shows the formation of columnar grains that are depleted in Al and O but rich in Mn (e.g. $MnAl_{0.3}O_{0.3}$ in Fig. S3g). The diffusion of O and depletion of Al induces near axial grain growth consistent with diffusion-induced grain boundary migration [32,33]. Much more work, that is beyond the scope of this paper - is needed if proper understanding is sought after.

SEM micrographs of an oxidized Fe_2AlB_2 sample at 900 °C for 96 h show a continuous $Al_{1.23}O_3$ layer, 5±2 µm thick (Fig. 5a and c). The EDS O:Al ratio of 3:1.23 is less than expected for Al_2O_3, even though the EDS was calibrated with an Al_2O_3 reference. The oxide composition is revealed by XPS to be $Al_4B_2O_9$ and not Al_2O_3 (Table 4). As discussed in the next section, the measured XPS Al:B molar ratio, at ≈ 2:1 (Table 4), is that of $Al_4B_2O_9$.

When combined with the XRD, EDS, and SEM results, it is reasonable to conclude that the passivating phase in this case is arguably $Al_4B_2O_9$ and not Al_2O_3. This, in turn, suggests that the Al and B are selectively

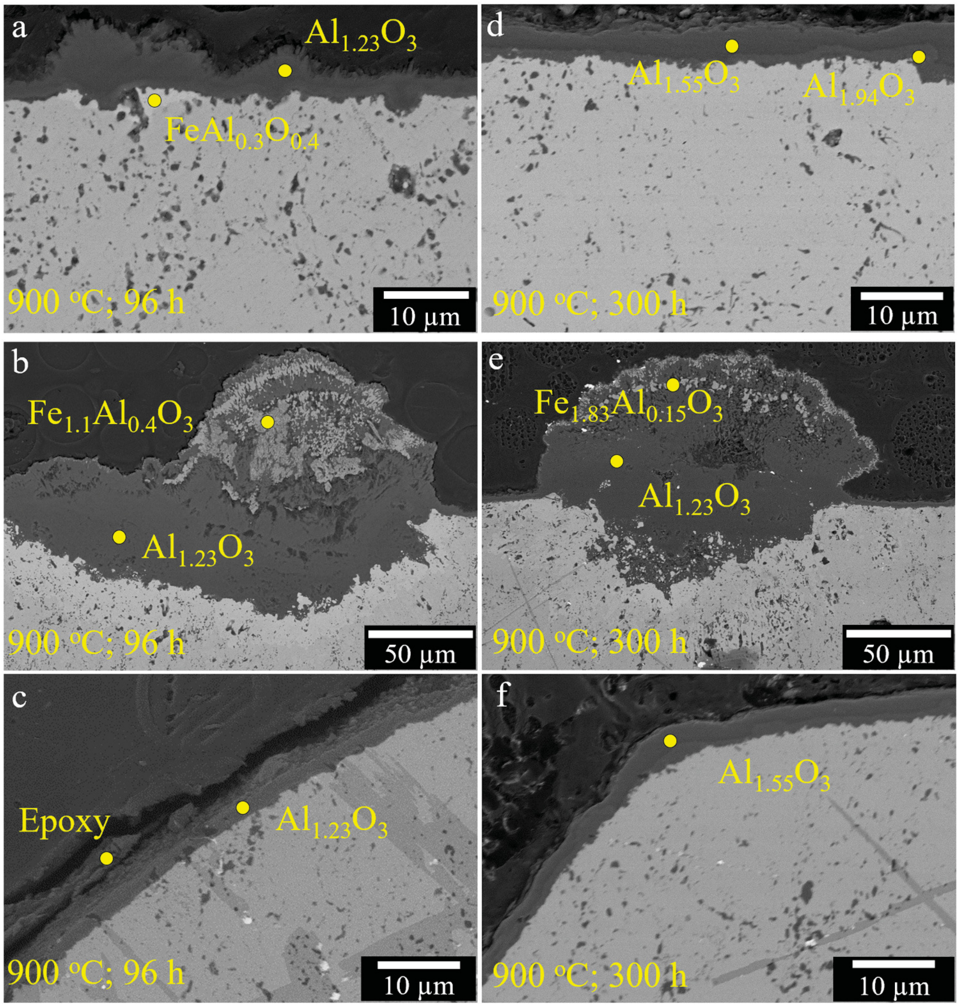

Fig. 5. Backscattered electron SEM micrographs of oxidized Fe_2AlB_2 polished cross-sections after isothermal oxidation in natural air at 900 °C for 96 h (left column) and 300 h (right column).

oxidized by diffusing outward. The lack of a Fe signal, in the outermost protective layer implies that oxidation did *not* occur by O diffusion inwards.

This layer also protected the corners; excellent adherence is observed at the corners with no sign of spallation (Fig. 5c). However, this layer was not uniform in thickness. In some sporadic locations, quite large, 50 ±20 μm nodules formed (Fig. 5b and e). According to EDS, their chemistry appeared to be $Fe_{1.83}Al_{0.15}O_3$ ($\sim Fe_2O_3$) (Fig. 5e) and/or a solid solution between Fe_2O_3 and Al_2O_3 viz. $Fe_{1.1}Al_{0.4}O_3$ (Fig. 5b).

Localized regions of $FeAl_{0.3}O_{0.4}$ (Fig. 5a) are also detected between the outer oxide layer and the substrate. Chemical inhomogeneities in the substrate most probably contribute to formation of the nodules (see Fig. 1), though more investigation is needed to confirm this conclusion. For example, Fe-rich regions could interfere with the formation of a protective $Al_4B_2O_9$ layer. The presence of Fe in the nodules implies that, in this case, the oxidation occurs by the inward diffusion of oxygen.

Most notably extending the oxidation time to 300 h at 900 °C (Fig. 5d-f) resulted in little growth of the baseline $Al_4B_2O_9$ layer to 5 ±2 μm (Fig. 5d). The same is true of the nodules; they do not appear to grow much with time (compare Fig. 5b and e).

The Al content in Fe-Al alloys must exceed 9 at% to form continuous Al_2O_3 layers [34,35]. Xu et al. and others further showed that the Al content must exceed 15–20 at.% to suppress Fe_2O_3 nodule formation at 800 °C [36,37]. Those findings are consistent with ours for Fe_2AlB_2 with a 20 at% Al (17 wt% Al) concentration. Fe_2AlB_2 formed continuous Al_2O_3 but sustained some Fe_2O_3 nodules.

The parabolic rate constants are $k_{p,w}$= $3.1\pm0.3 \times 10^{-6}$ and 6.2×10^{-9} $kg^2m^{-4}s^{-1}$ for Fe_2AlB_2 at 900 °C and Fe-10Al (i.e. 10 at% Al) at 1000 °C, respectively. The Al_2O_3 thicknesses were 5±2 and 10±2 μm for Fe_2AlB_2 after 96 h and Fe-10Al after 50 h, respectively [38]. The Fe_2O_3 nodules in Fe_2AlB_2 and Fe-10Al were 50±20 μm and 100±20 μm thick, respectively. Notably, $k_{p,w}$ is highly dependent on the Al content of Fe-Al alloys and ranges from 1.47×10^{-13} to 1.20×10^{-5} $kg^2m^{-4}s^{-1}$ [34,36, 39,40]. We note in passing, that the presence of Fe_2O_3 nodules in Fe-Al alloys indicates an inability to supply sufficient aluminum for the exclusive formation of Al_2O_3 scales [35].

After oxidation at 1000 °C for 96 h (Figs. S4a and b), the oxidation is catastrophic. EDS of the resulting oxides indicated a combination of an external bright Fe_2O_3-based ($Fe_{2.13}Al_{0.16}O_{2.8}$) layer below which a darker ~ $Al_4Fe_2O_{12}$ layer formed. The latter resulted from the combination of $Al_4B_2O_9$ and Fe_2O_3. The peaks for the former were prominent in the XRD patterns (Fig. 2b). In this case, thermal competition between the axial and lateral growth of $Al_4B_2O_9/\alpha{-}Al_2O_3$ inhibits passivation, such that a continuous lateral layer is not formed quickly enough to be protective.

3.4. Boron content of oxides formed on Mn_2AlB_2 and Fe_2AlB_2

To confirm the presence of B in the oxide layers, XPS spectra after 1 min of Ar sputtering were obtained for an oxidized Mn_2AlB_2 sample at 700 °C after 6 h. The Mn 3 s orbital peaks shown in Fig. 6a and e, before, and after, sputtering, respectively, display two peaks at binding

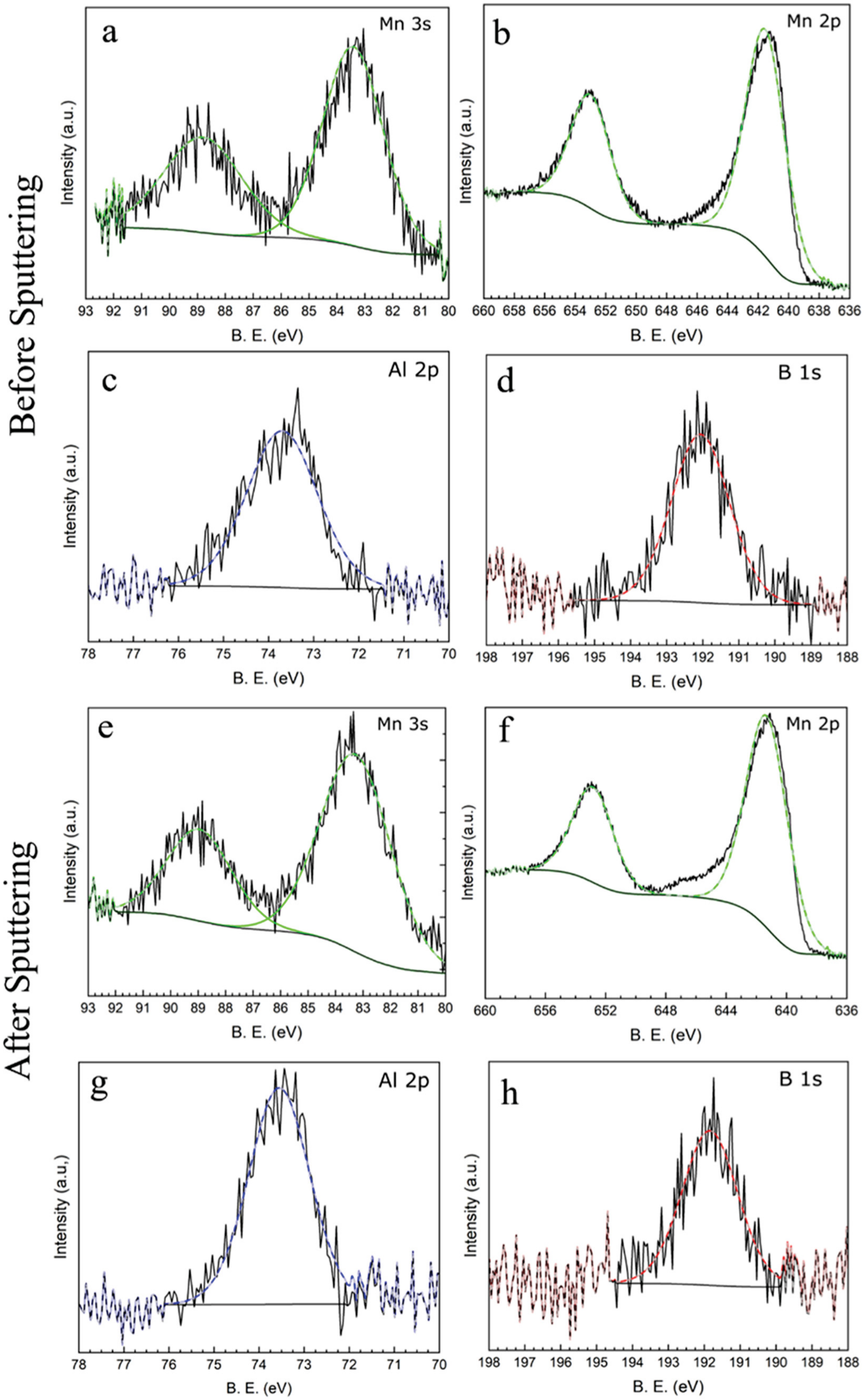

Fig. 6. XPS spectra with fits of oxidized Mn_2AlB_2 at 700 °C after 6 h, a-d) before, and e–h) after sputtering.

energies, BE, of 83.50 eV and 89.00 eV, with a peak separation of 5.50 eV, which is consistent with Mn_2O_3 [41,42]. In the Mn 2p region (Fig. 6b and f), two peaks at BEs of 641.00 eV and 653.00 eV are present. These results were consistent with the presence of Mn_2O_3.

The Al spectra (Fig. 6c and g) show a peak at BE 73.75 eV consistent with Al_2O_3 peaks in the 74.00–75.00 eV range [43,44]; the Al metal peak is typically at 72.50–73.00 eV [45,46]. The B spectra (Fig. 6d and h) show a peak at BE of 192.84 eV, consistent with B_2O_3 [47].

The XPS chemical compositions of the sputtered oxidized Mn_2AlB_2 sample at 700 °C after 6 h are listed in Table 4. The majority element is Mn, with smaller amounts of Al and B. If one assumes the Al is in solid solution in the Mn_2O_3 phase, then the final oxide composition is $Mn_{27}Al_4O_{57}$ (Table 4). This implies that x in $Mn_{2\text{-}x}Al_xO_3$ is ≈ 0.2. Therefore, B is present as B_2O_3.

The XPS spectra (not shown) of the Fe-containing sample oxidized at 900 °C for 24 h only showed peaks for B, Al, and O at a molar ratio of 13:25:62 (Table 4), which is consistent with the chemistry of the ternary, $Al_4B_2O_9$. The lack of an Fe signal simply reflects that it is below the surface. The XRD results (Fig. 2b) are unambiguous as to the presence of Fe_2O_3

3.5. *Predicted weight gains*

To shed more light on the oxidation process, the scale thicknesses, Δ*x*, were estimated from the micrographs shown in Figs. 4 and 5, converted to a predicted weight gain, and compared to the measured weight gains. The results are shown in Fig. 7a and b for Mn_2AlB_2 and Fe_2AlB_2, respectively. The O_2 weight fraction of each individual oxide listed on Fig. 2a was multiplied by the average density of that oxide. For Mn_2AlB_2, Mn_2O_3, and $Al_4B_2O_9/Al_{18}B_4O_{33}$ thicknesses $\Delta x_{Mn_2O_3}$ and $\Delta x_{Al_4B_2O_9}$, measured from Fig. 4, were multiplied by their respective densities and O_2 weight fractions then summed together to predict the weight gain.

For Fe_2AlB_2, a similar procedure was followed for Fe_2O_3 and $Al_4B_2O_9/Al_{18}B_4O_{33}$ listed on Fig. 2b using thicknesses $\Delta x_{Fe_2O_3}$ and $\Delta x_{Al_4B_2O_9}$, measured from Fig. 5. However, Fe_2O_3 forms isolated nodules instead of a continuous layer; therefore, the nodule thickness is multiplied by its total area fraction, average density and O_2 weight fraction to estimate its weight gain contribution before summation to the contribution of $Al_4B_2O_9$.

The results showed that, in general, the predicted weight gain for Mn_2AlB_2 at 700 °C was in good agreement with the measured weight gain (Fig. 7a). This implies that there was little solubility of O in the substrate.

For Fe_2AlB_2 at 900 °C, predicted weight gain is in agreement with the actual weight gain within the uncertainty (Fig. 7b). The Fe_2O_3 nodules vary in thickness which leads to uncertainty in the predicted weight gain. Note that the α-Al_2O_3 and Fe_2O_3 peaks in Fig. 2b arise from the nodules.

4. Conclusions

In this present work, the isothermal oxidation of bulk Mn_2AlB_2 in air in the 700–900 °C temperature range for up to 150 h was investigated. After oxidation at 700 °C, a pseudo-protective layer of $Mn_{2\text{-}x}Al_xO_3$ forms. At 0.13, the oxidation rate exponent at 700 °C is exceedingly low. At 800–900 °C, oxidation is catastrophic owing to the oxide spallation.

The Fe_2AlB_2 samples oxidized at 900 °C form a passivating $Al_4B_2O_9$ layer based on XPS chemistries and EDS compositions. This layer does not appear to spall and is protective even at the corners. Beyond 60 h of oxidation at 900 °C, the oxidation rate exponent, n, is 0.42–0.46. Oxidation at 800 °C and 1000 °C is rapid because no such layer forms for reasons that are not clear.

CRediT authorship contribution statement

Michel W. Barsoum: Writing – review & editing, Supervision, Resources, Project administration, Methodology, Investigation, Funding acquisition, Formal analysis, Conceptualization. **Mary Qin Hassig:** Writing – original draft, Formal analysis, Data curation. **Or Messer:** Writing – original draft, Methodology, Formal analysis, Data curation. **Maxim Sokol:** Writing – review & editing, Formal analysis, Data curation, Conceptualization. **Tarek Aly Elmeligy:** Writing – review & editing, Writing – original draft, Visualization, Software, Resources, Methodology, Investigation, Formal analysis, Data curation, Conceptualization.

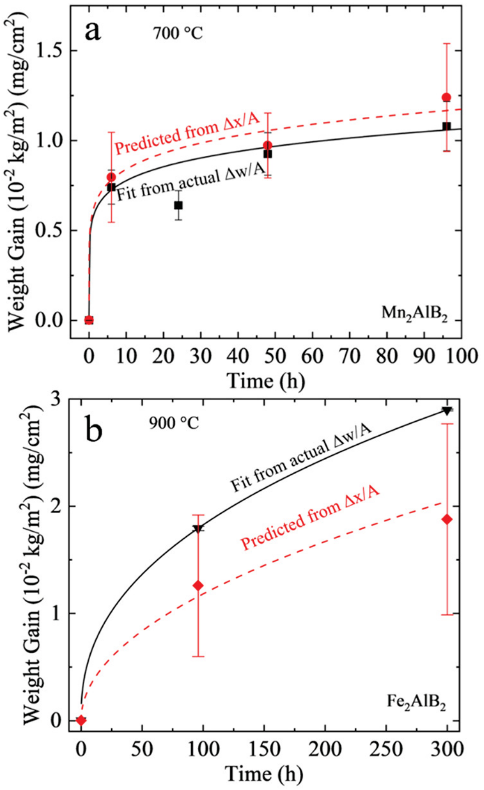

Fig. 7. Weight gain vs time (dashed lines) for a) Mn_2AlB_2 and b) Fe_2AlB_2 predicted from oxide thicknesses Δx/A in Figs. 4–5, compared to measured weight gain fits from furnace results (solid lines).

Declaration of interests

The authors declare the following financial interests/personal relationships which may be considered as potential competing interests, Michel W. Barsoum reports financial support was provided by National Science Foundation. Michel W. Barsoum reports a relationship with National Science Foundation that includes: funding grants. Tarek Aly ElMeligy reports a relationship with National Science Foundation that includes: funding grants.

Acknowledgements

This work was funded by the National Science Foundation, NSF, DMREF program (1729335). The authors extend their thanks to S. Kota for sample preparation, data collection and consultation. The authors thank D.Barbash for assistance with the XRD hardware information.

Appendix A. Supporting information

Supplementary data associated with this article can be found in the online version at doi:10.1016/j.jeurceramsoc.2024.116801.

References

[1] S. Kota, M. Sokol, M.W. Barsoum, A progress report on the MAB phases: atomically laminated, ternary transition metal borides, Int. Mater. Rev. 65 (2020) 226–255.

[2] H.J. Becher, K. Krogmann, E. Peisker, Über das ternäre borid Mn_2AlB_2, Z. F. üR. Anorg. Und Allg. Chemi. 344 (1966) 140–147.

[3] W. Jeitschko, The crystal structure of Fe_2AlB_2, Acta Crystallogr. Sect. B Struct. Crystallogr. Cryst. Chem. 25 (1969) 163–165.

[4] Y.B. Kuzma, N.F. Chaban, Crystal structure of the compound Fe_2AlB_2, Izvest. Akad. Nauk Sssr Neorg. Mater. 5 (1969) 384–385.

[5] M. Ade, H. Hillebrecht, Ternary Borides Cr_2AlB_2, Cr_3AlB_4, and Cr_4AlB_6: the first members of the series $(CrB_2)nCrAl$ with $n = 1, 2, 3$ and a unifying concept for ternary borides as MAB-phases, Inorg. Chem. 54 (2015) 6122–6135.

[6] S. Kota, Y. Chen, J. Wang, S.J. May, M. Radovic, M.W. Barsoum, Synthesis and characterization of the atomic laminate Mn_2AlB_2, J. Eur. Ceram. Soc. 38 (2018) 5333–5340.

[7] J. Cedervall, M.S. Andersson, D. Iuşan, E.K. Delczeg-Czirjak, U. Jansson, P. Nordblad, M. Sahlberg, Magnetic and mechanical effects of Mn substitutions in $AlFe_2B_2$, J. Magn. Magn. Mater. 482 (2019) 54–60.

[8] J. Liu, S. Li, B. Yao, J. Zhang, X. Lu, Y. Zhou, Thermal stability and thermal shock resistance of Fe_2AlB_2, Ceram. Int. 44 (2018) 16035–16039.

[9] L. Verger, S. Kota, H. Roussel, T. Ouisse, M.W. Barsoum, Anisotropic thermal expansions of select layered ternary transition metal borides: MoAlB, Cr_2AlB_2, Mn_2AlB_2, and Fe_2AlB_2, J. Appl. Phys. 124 (2018) 205108, https://doi.org/10.1063/1.5054379.

[10] S. Kota, L. Verger, V. Natu, M. Sokol, M.W. Barsoum, Thermal stability of the nanolayered Fe_2AlB_2 in nitrogen and argon atmospheres, J. Am. Ceram. Soc. 104 (2021) 733–739.

[11] A. Benamor, Y. Hadji, S. Kota, N. Chiker, L. Liu, A. Haddad, T. Sahraoui, G. Ying, M. Hadji, Friction and wear characteristics of the nanolaminated ternary transition metal boride: Mn_2AlB_2, Wear 492–493 (2022) 204232.

[12] S. Kota, E. Zapata-Solvas, Y. Chen, M. Radovic, W.E. Lee, M.W. Barsoum, Isothermal and cyclic oxidation of MoAlB in air from 1100°C to 1400°C, J. Electrochem. Soc. 164 (2017) C930–C938.

[13] Y. Ren, F.Z. Dai, H. Xiang, X. Wang, L. Sun, Y. Zhou, Mechanical and thermal properties of light weight boron-mullite Al_5BO_9, J. Am. Ceram. Soc. 103 (2020) 5939–5951.

[14] N. Doebelin, R. Kleeberg, Profex: a graphical user interface for the Rietveld refinement program BGMN, J. Appl. Crystallogr. 48 (2015) 1573–1580.

[15] J. Bergmann, P. Friedel, R. Kleeberg, BGMN - a new fundamental parameters based rietveld program for laboratory X-ray sources, it's use in quantitative analysis and structure investigations, IUCr Comm. Powder Diffr. Newsl. 20 (1998) 5–8.

[16] G. Greczynski, L. Hultman, C 1s peak of adventitious carbon aligns to the vacuum level: dire consequences for material's bonding assignment by photoelectron spectroscopy, ChemPhysChem 18 (2017) 1507–1512.

[17] M. Ilatovskaia, O. Fabrichnaya, Critical assessment and thermodynamic modeling of the Al-Mn-O system, J. Alloy. Compd. 884 (2021).

[18] T. Ranganathan, B.E. Mackean, A. Muan, The system manganese oxide–alumina in air, J. Am. Ceram. Soc. 45 (1962) 279–281.

[19] Y.-B. Kang, I.-H. Jung, Thermodynamic modeling of oxide phases in the Mn-O System, Metall. Mater. Trans. E 3 (2016) 156–170.

[20] M. Wang, B. Sundman, Thermodynamic assessment of the Mn-O system, Metall. Trans. B. 23 (1992) 821–831.

[21] M.W. Barsoum, Fundamentals of Ceramics, IOP Publishing Ltd, 2003.

[22] K. Terayama, M. Ikeda, Study on thermal decomposition of MnO_2 and Mn_2O_3 by thermal analysis, Trans. Jpn. Inst. Met 24 (1983) 754–758.

[23] H. Schmalzried, W. Laqua, Multicomponent oxides in oxygen potential gradients, Oxid. Met. 15 (1981) 339–353.

[24] G.J. Yurek, H. Schmalzried, Interdiffusion in (A,B)O-type Solid Solutions and the Validity of Darken's Equation, Ber. Der Bunsenges. F. üR. Phys. Chem. 78 (1974) 1379–1386.

[25] H. Schmalzried, Diffusion in oxides, React. Solids 5 (1988) 269–278.

[26] H. Schmalzried, Demixing, decomposition and degradation of oxides in chemical potential gradients, J. Chem. Soc. Faraday Trans. 86 (1990) 1273.

[27] T.A. ElMeligy, E. Epifano, M. Sokol, G. Hug, M. Hans, J.M. Schneider, M. W. Barsoum, Isothermal Oxidation of $Ti_3Al_{0.6}Ga_{0.4}C_2$ MAX Phase Solid Solution in Air at 1000 °C to 1300 °C, J. Electrochem. Soc. 169 (2022) 031510.

[28] D.J. Tallman, B. Anasori, M.W. Barsoum, A critical review of the oxidation of Ti_2AlC, Ti_3AlC_2 and Cr_2AlC in Air, Mater. Res. Lett. 1 (2013) 115–125.

[29] S. Basu, N. Obando, A. Gowdy, I. Karaman, M. Radovic, Long-term oxidation of Ti_2AlC in air and water vapor at 1000–1300 °C temperature range, J. Electrochem. Soc. 159 (2011) C90–C96.

[30] W.G. Fahrenholtz, The ZrB_2 volatility diagram, J. Am. Ceram. Soc. 88 (2005) 3509–3512.

[31] T.A. Parthasarathy, R.A. Rapp, M. Opeka, R.J. Kerans, A model for the oxidation of ZrB_2, HfB_2 and TiB_2, Acta Mater. 55 (2007) 5999–6010.

[32] R.W. Balluffi, J.W. Cahn, Mechanism for diffusion induced grain boundary migration, Acta Met. 29 (1981) 493–500.

[33] G.X. Liu, Z.M. Guan, Diffusion induced grain boundary migration, Defect Diffus. Forum 150– 151 (1997) 95–134.

[34] P. Tomaszewicz, G.R. Wallwork, Observations of nodule growth during the oxidation of pure binary iron-aluminum alloys, Oxid. Met. 19 (1983) 165–185.

[35] R. Prescott, M.J. Graham, The oxidation of iron-aluminum alloys, Oxid. Met. 38 (1992) 73–87.

[36] X. Xu, H. Wei, J. Xiang, L. Wang, M. Liu, H. Zhang, D. Men, J. An, Oxidation mechanism of three Fe-Al alloys with and without addition of 0.1 at% yttrium at 800 °C, J. Rare Earths. 38 (2020) 1126–1130.

[37] M. Sakiyama, P. Tomaszewicz, G.R. Wallwork, Oxidation of iron-nickel aluminum alloys in oxygen at 600-800° C, Oxid. Met. 13 (1979) 311–330.

[38] Z.G. Zhang, F. Gesmundo, P.Y. Hou, Y. Niu, Criteria for the formation of protective Al2O3 scales on Fe–Al and Fe–Cr–Al alloys, Corros. Sci. 48 (2006) 741–765.

[39] H.A. Ahmed, W.W. Smeltzer, Oxidation properties of Fe-Al alloys (1.5–5 a/o Al) in oxygen at 1173 K, J. Electrochem. Soc. 133 (1986) 212–216.

[40] R.E. Grace, A.U. Seybolt, Selective oxidation of Al from an Al -Fe alloy, J. Electrochem. Soc. 105 (1958) 582.

[41] E.S. Ilton, J.E. Post, P.J. Heaney, F.T. Ling, S.N. Kerisit, XPS determination of Mn oxidation states in Mn (hydr)oxides, Appl. Surf. Sci. 366 (2016) 475–485.

[42] J.L. Junta, M.F. Hochella, Manganese (II) oxidation at mineral surfaces: a microscopic and spectroscopic study, Geochim. Cosmochim. Acta 58 (1994) 4985–4999.

[43] V. Natu, S.S. Kota, M.W. Barsoum, X-ray photoelectron spectroscopy of the MAB phases, MoAlB, M_2AlB_2 ($M = Cr, Fe$), Cr_3AlB_4 and their binary monoborides, J. Eur. Ceram. Soc. 40 (2020) 305–314.

[44] I. Iatsunskyi, M. Kempi Nski, M. Jancelewicz, K. Załe, S. Jurga, V. Smyntyna, Structural and XPS Characterization of ALD Al_2O_3 Coated Porous Silicon, Elsevier, 2015.

[45] C.F. McConville, D.L. Seymour, D.P. Woodruff, S. Bao, Synchrotron radiation core level photoemission investigation of the initial stages of oxidation of Al(111), Surf. Sci. 188 (1987) 1–14.

[46] C. Hinnen, D. Imbert, J.M. Siffre, P. Marcus, An in situ XPS study of sputter-deposited aluminium thin films on graphite, Appl. Surf. Sci. 78 (1994) 219–231.

[47] N.F. Rosli, M.Z.M. Nasir, N. Antonatos, Z. Sofer, A. Dash, J. Gonzalez-Julian, A. C. Fisher, R.D. Webster, M. Pumera, MAX and MAB phases: two-dimensional layered carbide and boride nanomaterials for electrochemical applications, ACS Appl. Nano Mater. 2 (2019) 6010–6021.